



CHALMERS
UNIVERSITY OF TECHNOLOGY

Structural Battery Electrolytes Based on a Cross-Linked Methacrylate Polymer and a Protic Ionic Liquid: Is There an Optimal Composition?

Downloaded from: <https://research.chalmers.se>, 2026-05-09 13:42 UTC

Citation for the original published paper (version of record):

Abdou, N., Pipertzis, A., Chaudhary, R. et al (2025). Structural Battery Electrolytes Based on a Cross-Linked Methacrylate Polymer and a Protic Ionic Liquid: Is There an Optimal Composition?. *Advanced Energy and Sustainability Research*, 6. <http://dx.doi.org/10.1002/aesr.202500013>

N.B. When citing this work, cite the original published paper.

Structural Battery Electrolytes Based on a Cross-Linked Methacrylate Polymer and a Protic Ionic Liquid: Is There an Optimal Composition?

Nicole Abdou,* Achilleas Pipertzis, Richa Chaudhary, Lars Evenäs, Johanna Xu, Leif E. Asp, Jan Swenson, and Anna Martinelli*

Within the development of structural batteries, finding the optimal electrolyte composition, that is, one that offers both high ionic conductivity and mechanical stiffness, is essential. Structural batteries are multifunctional composites able to store electrical energy within load-bearing elements of devices. Their use results in a significant mass reduction, thereby improving fuel efficiency and enabling a shift to sustainable energy. In this work, structural battery electrolytes consisting of a methacrylate-based polymer, 1-ethylimidazolium bis(trifluoromethylsulfonyl)imide protic ionic liquid, and a lithium salt are investigated. Interestingly, the transport properties of the confined liquid electrolyte seem primarily limited by the percolation of the polymer network. Furthermore, upon confinement, a decrease in the glass transition temperature of the polymer phase and weaker intermolecular interactions are observed, which correlate to faster local dynamics. The self-diffusivity of the Li ions keeps high with respect to the other diffusing ions and tends to decouple from the anions upon increased temperature. The composite sample with 50 wt% of liquid electrolyte shows an ionic conductivity of $\approx 0.1 \text{ mS cm}^{-1}$ with a shear storage modulus of $\approx 150 \text{ MPa}$ and was thus selected for proof-of-concept tests by electrochemical methods. Overall, this comprehensive study highlights the versatility of these biphasic systems for various applications.


the low melting temperature, and the relatively high ionic conductivity in combination with a very high ionic density. This set of properties makes ionic liquids appealing for use in energy-related devices, such as Li-ion batteries, fuel cells, and supercapacitors.^[4,5] In this context, the subclass of protic ionic liquids has been less studied than the aprotic counterparts, yet they emerge as promising alternatives.^[6,7] Protic ionic liquids have an exchangeable proton, typically on the cation, which participates in extended hydrogen-bonded networks thereby resulting in stronger intermolecular interactions with effects also on the transport and thermal properties. The solubility of a Li salt and the mobility of ions may also be affected in the environment of a protic ionic liquid.^[8,9] Moreover, protic ionic liquids are obtained by a simple procedure via proton transfer from a Brønsted acid to a Brønsted base in a neutralization reaction, which is more straightforward than the multistep reaction needed to obtain aprotic ionic liquids.^[10]

1. Introduction

Ionic liquids have emerged as a promising class of materials that, also known as molten salts, have a melting temperature below $100 \text{ }^\circ\text{C}$.^[1,2] By varying the cation/anion combination, many properties of ionic liquids can be tuned,^[3] the properties exploited the most being the high chemical and thermal stability,

When used in energy devices, ionic liquids can be incorporated into a solid material, which can be of organic or inorganic nature, to avoid leakage. The resulting hybrid systems are also known as polymer electrolytes or ionogels. Watanabe and colleagues first proposed the synthesis of an ionogel via a radical polymerization of a vinylic monomer in an ionic liquid medium.^[11] Since then, several other works have been reported

N. Abdou, L. Evenäs, A. Martinelli
Department of Chemistry and Chemical Engineering
Chalmers University of Technology
41296 Gothenburg, Sweden
E-mail: nicole.abdou@chalmers.se; anna.martinelli@chalmers.se

 The ORCID identification number(s) for the author(s) of this article can be found under <https://doi.org/10.1002/aesr.202500013>.

© 2025 The Author(s). Advanced Energy and Sustainability Research published by Wiley-VCH GmbH. This is an open access article under the terms of the Creative Commons Attribution License, which permits use, distribution and reproduction in any medium, provided the original work is properly cited.

DOI: 10.1002/aesr.202500013

A. Pipertzis, J. Swenson
Department of Physics
Chalmers University of Technology
41296 Gothenburg, Sweden

R. Chaudhary, L. E. Asp
Department of Industrial and Materials Science
Wallenberg Initiative Material Science for Sustainability
Chalmers University of Technology
41258 Gothenburg, Sweden

J. Xu
Department of Industrial and Materials Science
Chalmers University of Technology
41258 Gothenburg, Sweden

on the synthesis, properties, and application of ionogels. An archetypical polymer used to realize Li-ion conducting materials is poly(ethylene oxide) (PEO), which has been mainly used in Li-ion batteries.^[12,13] The motion of Li ions in such a polymer electrolyte is coupled with the segmental motion of PEO chains and is further enhanced at higher temperatures and in the amorphous regions of the polymer.^[14] To improve the mechanical and transport properties of PEO-based systems, strategies have been proposed such as the inclusion of nano-sized fillers or the formation of localized amorphous regions.^[15] Still, the ionic conductivity and the mechanical properties in these systems remain inversely proportional to each other. Another competitive material concept consists of a biphasic system, in which the polymer phase provides mechanical stiffness and the (ionic) liquid phase provides ionic conductivity.^[16,17]

The structural battery is a good example of device that uses a phase-separated electrolyte, more specifically based on a liquid electrolyte trapped within a cured polymer (a resin). The phase separation in the case of a structural battery electrolyte (SBE) is due to the difference in solubility between the monomer and the cured polymer, which results in a polymerization-induced phase separation.^[18] Structural batteries are promising composite materials that are taking space in the field of Li-ion batteries^[19–23] and consist of interpenetrated multifunctional components: 1) carbon fibers that enable lithium ions insertion and electrical conductivity and 2) a polymer network that provides mechanical load transfer while confining 3) the liquid electrolyte responsible for ion transport. This unique design enables the storage of electrical energy within load-bearing components of a device or a part of a vehicle.^[24,25] One key challenge to achieve multifunctionality in structural batteries is the design of a suitable SBE, exhibiting simultaneous high ionic conductivity and mechanical stiffness.^[26–29]

Several ionic liquid-based structural battery electrolytes have been reported in the literature.^[30–36] Shirshova et al.^[30] detailed the synthesis of a structural battery electrolyte consisting of the aprotic ionic liquid 1-ethyl-3-methylimidazolium bis(trifluoromethylsulfonyl)imide [C₂C₄Im][TFSI] and three distinct epoxy resins. By varying the type and weight fraction of the resin phase, an optimal formulation exhibited a Young's modulus of 0.2 GPa and an ionic conductivity of 0.8 mS cm⁻¹ at 20 °C. Moreover, Kwon et al.^[31] reported the synthesis of multifunctional SBEs based on an epoxy resin, the [C₂C₄Im][TFSI] aprotic ionic liquid, and Li-TFSI salt. This SBE revealed a good mechanical strength of about 1 GPa at 25 °C and an ionic conductivity in the order of 0.1 mS cm⁻¹. In a recent work from our group, an extension of this concept was proposed by considering a protic ionic liquid instead (i.e., 1-ethylimidazolium bis(trifluoromethylsulfonyl) imide), combined with a methacrylate-based resin (ethoxylated bisphenol A dimethacrylate polymer) in a 50 wt% mixture.^[37]

To gain further knowledge of these new types of systems and to find strategies for optimization, the impact of composition on all relevant properties of a SBE—more specifically the thermal, transport, and morphological properties—is here thoroughly investigated. To make such an investigation, a complete set of experimental methods is used, including nitrogen sorption and scanning electron microscopy (SEM), broadband dielectric spectroscopy (BDS), diffusion nuclear magnetic resonance (NMR) spectroscopy, vibrational spectroscopy (Raman), differential scanning calorimetry (DSC), and temperature-modulated

DSC (TM-DSC), as well as rheology. In addition, electrochemical tests were performed to better understand the potential use of these composites.

2. Results and Discussion

The SBEs studied here consist of a solid polymer phase based on ethoxylated Bisphenol A dimethacrylate (its abbreviation being DMA throughout the whole text) and a liquid electrolyte phase. This liquid electrolyte consists of a 0.2 M solution of the salt lithium bis(trifluoromethane)sulfonimide (LiTFSI) in the protic ionic liquid 1-ethylimidazolium bis(trifluoromethyl sulfonyl) imide [C₂HIm][TFSI]; its abbreviation is SIL throughout the whole text (from salt in ionic liquid), which is used for labeling the samples (see also Table 3 in Section 4.2). This particular cation–anion combination for the ionic liquid results in lower viscosity and, thus, higher ionic conductivity compared to other ion pairs.^[38,39] The polymer electrolytes are obtained by a polymerization-induced phase separation in the presence of a thermal initiator (**Figure 1**), the detailed synthesis procedure and the exact amount of precursors used being described in Table 3. As also mentioned in the Introduction, the mass ratio between the polymer and the liquid electrolyte phase was systematically varied, to analyze its effect on the physicochemical properties of the obtained SBEs. Throughout the following text, samples are named DMA_xSIL_{1–x}, where *x* represents the DMA mass ratio and varies between 0, 0.3, 0.4, 0.5, 0.6, 0.7, and 1; the neat polymer sample is labeled DMA while the neat liquid electrolyte is labeled SIL.

2.1. Increased Porosity with Higher Liquid Content

The morphological properties of the SBE samples after extraction of the liquid phase were investigated via nitrogen sorption experiments and scanning electron microscopy. The confined SIL phase was removed following a 24 h ethanol washing procedure, using a soxhlet apparatus. The nitrogen sorption isotherms of the extracted SBE samples (**Figure 1c**) show low porosity for the materials synthesized with a low SIL content (30 and 40 wt%). However, porosity—in terms of specific surface area, pore volume, and pore diameter—increases with the SIL content, reaching a maximum for the DMA_{0.3}SIL_{0.7} sample (see Table S1, Supporting Information, for further details). The extracted DMA_{0.5}SIL_{0.5}, DMA_{0.4}SIL_{0.6}, and DMA_{0.3}SIL_{0.7} samples show type IV isotherms with H3-type hysteresis loops, which confirm the presence of well-connected pores. These isotherms suggest also the presence of large pores which are not completely filled with nitrogen. Moreover, the application of the Barret–Joyner–Halenda (BJH) method upon adsorption reveals that all studied samples display a very wide pore distribution (see inset in **Figure 1c**). However, given the complexity of these hybrid systems and the very wide pore distribution, focus should be on the composition trends rather than on absolute values. The SEM images confirm an increased porosity upon higher content of liquid electrolyte; for example, the DMA_{0.4}SIL_{0.6} sample shows wider architecture and larger pores compared to DMA_{0.7}SIL_{0.3} (**Figure 1d**). Overall, the current study reveals that, despite the wide pore distribution and the strong correlation between

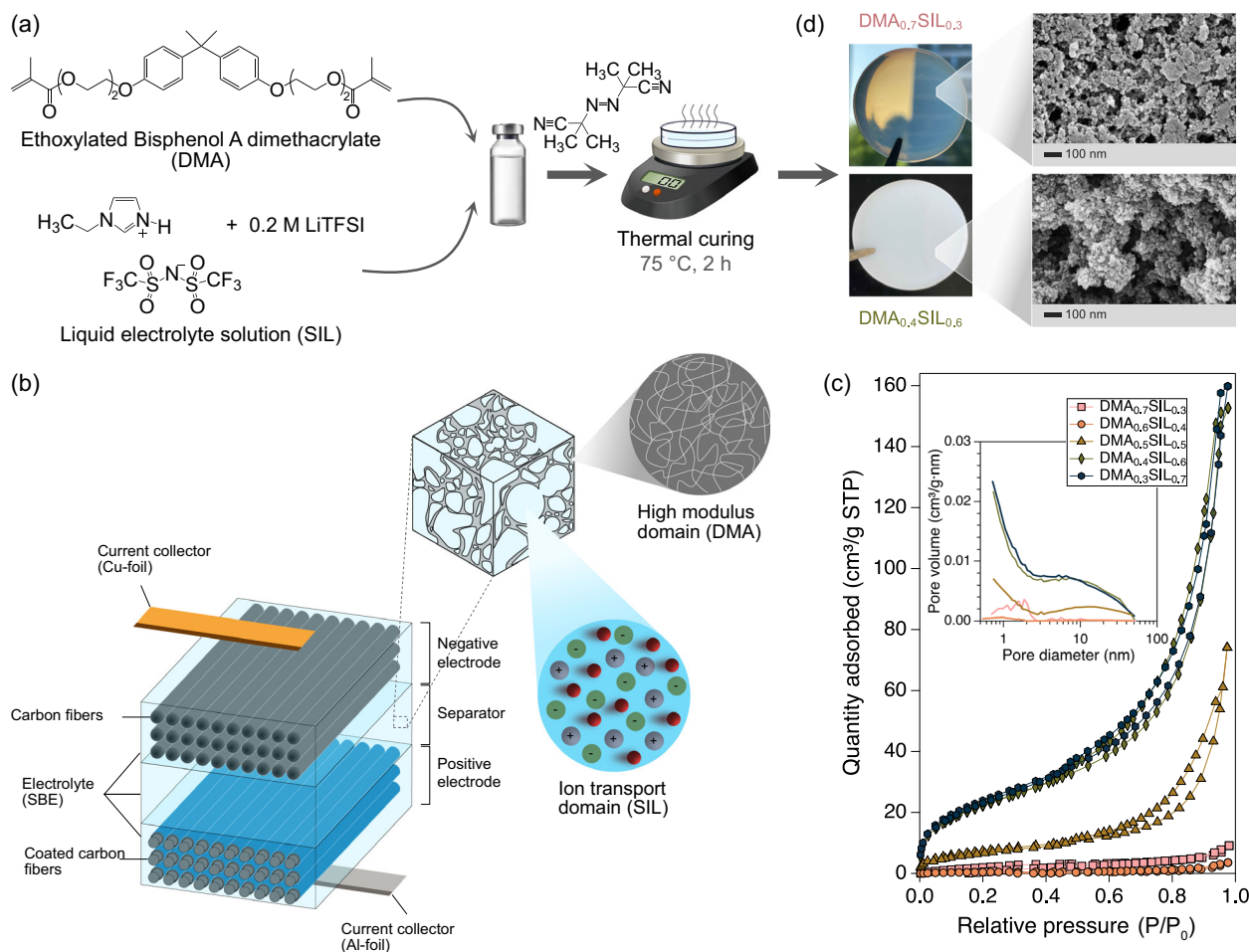


Figure 1. a) Details of the SBEs synthesis procedure. b) Illustration of the SBEs concept. c) Nitrogen sorption isotherms at 77 K of different SBE samples after extraction of the liquid phase. The inset in (c) shows the micro/mesopores size distribution determined using the Barrett–Joyner–Halenda (BJH) method upon adsorption. d) SEM images of the cross section of samples $\text{DMA}_{0.7}\text{SIL}_{0.3}$ (top) and $\text{DMA}_{0.4}\text{SIL}_{0.6}$ (bottom).

porosity and SIL content, most of the pore volume in SBE samples is concentrated in the sub-10 nm range. This emphasizes the crucial role played by small pores in the ionic transport properties of these composites.

2.2. Decreased Crystallinity upon Confinement

The phase behavior of the different SBE samples was investigated by DSC and compared to that of the bulk SIL, as summarized in **Figure 2** which shows clear compositional trends. Two glass transition temperatures (T_g^{DMA} and T_g^{SIL}) were detected, which can be associated with the vitrification of the liquid ion-conducting phase (lower value, T_g^{SIL}) and the solid polymer phase (higher value, T_g^{DMA}), respectively.^[37] In the temperature range between these two T_g values, most DSC curves upon heating show two first-order phase transitions, that is, cold-crystallization and melting of the crystalline part of the SIL phase. All calorimetric results are summarized in **Table 1**.

The T_g of the confined liquid phase is lower than that of the bulk SIL (**Figure 2c**), highlighting the effect of geometrical

confinement, which has been correlated to weak interfacial interactions between DMA and SIL and faster local dynamics.^[37] A deeper understanding of the significance of T_g and the relaxation dynamics within amorphous domains can be obtained from dielectric measurements. This involves an examination of the viscosity-related ion dynamics, as detailed in **Figure S4**, Supporting Information. The crystalline part of the SIL is also affected upon confinement, with the enthalpy of melting decreasing systematically from the bulk value (**Table 1**). As discussed below, the lower degree of crystallinity has a direct impact on the temperature dependence of dc-conductivity.

2.3. Faster Dynamics and Lower Activation Energy with Increased SIL Content

2.3.1. Ionic Conductivity

The ionic conductivity of the different samples was measured as a function of temperature in the frequency range from

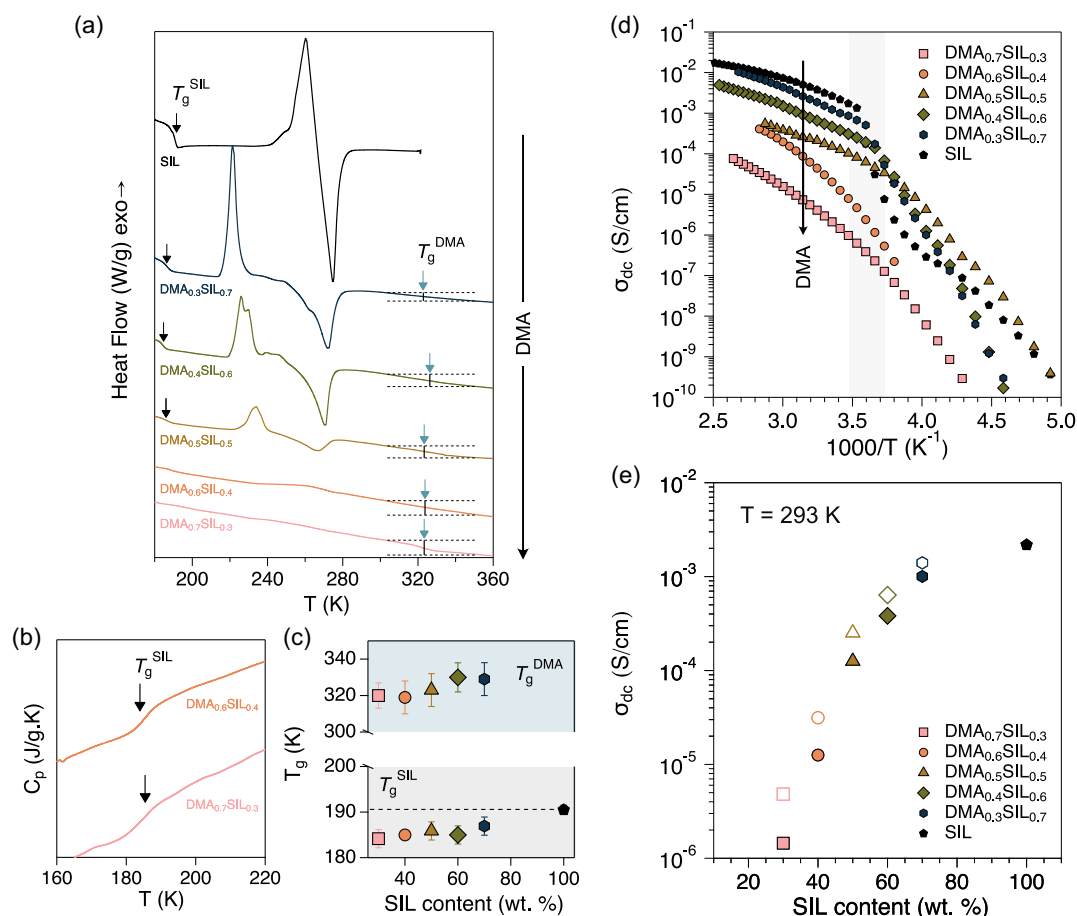


Figure 2. a) DSC thermograms for the SBEs samples and the bulk SIL. b) Temperature-modulated DSC curves for $\text{DMA}_{0.6}\text{SIL}_{0.4}$ (top) and $\text{DMA}_{0.7}\text{SIL}_{0.3}$ (bottom). c) Glass transition temperatures as a function of SIL content. The dashed line in (c) is simply a guide for the eyes. d) Ionic conductivity of the SBE samples and the bulk SIL. e) Composition dependence of the as-measured (filled symbols) and compensated (open symbols, calculated using Equation (1)) ionic conductivity at 293 K.

Table 1. Glass transition (T_g), cold crystallization (T_{cc}), and melting (T_m) temperatures as well as enthalpy change of melting (ΔH_m) obtained from DSC measurements.

Sample	T_g^{SIL} [K]	T_{cc}^{SIL}	T_m^{SIL} [K]	ΔH_m^{SIL} [J g ⁻¹]	T_g^{DMA} [K]
SIL	190 ± 1	260 ± 1	275.0 ± 0.5	28 ± 5	n/a
$\text{DMA}_{0.3}\text{SIL}_{0.7}$	187 ± 2	224 ± 3	271.5 ± 0.5	27 ± 3	329 ± 9
$\text{DMA}_{0.4}\text{SIL}_{0.6}$	185 ± 2	227 ± 2	269 ± 2	22 ± 3	320 ± 8
$\text{DMA}_{0.5}\text{SIL}_{0.5}$	186 ± 2	231 ± 2	268 ± 2	8 ± 1	323 ± 9
$\text{DMA}_{0.6}\text{SIL}_{0.4}$	185 ± 1 ^{a)}	n/a	n/a	n/a	319 ± 9
$\text{DMA}_{0.7}\text{SIL}_{0.3}$	184 ± 2 ^{a)}	n/a	n/a	n/a	320 ± 6

^{a)}Extracted from TM-DSC.

10^{-2} to 10^7 Hz. The dc-conductivity values were extracted from the plateau regimes of the frequency-dependent real part of conductivity (see Figure S3a, Supporting Information) and are shown as a function of inverse temperature in Figure 2d. Shown in an Arrhenius plot, these conductivity values reveal

some sharp trend changes, which are attributed to solid-liquid phase transitions (in agreement with results from DSC). These step changes are less pronounced for the samples with a lower crystallinity, such as $\text{DMA}_{0.5}\text{SIL}_{0.5}$.

Figure 2e also reveals that at ambient temperature ($T = 293$ K, or any temperature above T_m), the dc-conductivity increases with the content of SIL, reflecting both the growth in pore size (hence the change in morphology) and the increased concentration of ionic species. For comparison purposes, the as-measured conductivity values (σ_{meas}) were compensated considering the weight fraction (w_{SIL}) of the ion-conducting phase, using the following equation

$$\sigma_{\text{comp}} = \frac{\sigma_{\text{meas}}}{w_{\text{SIL}}} \quad (1)$$

Importantly, the compensated dc-conductivity value of $\text{DMA}_{0.3}\text{SIL}_{0.7}$ reaches almost the bulk value of SIL (Figure 2e), suggesting a transport of ions through large, well-connected pores that enables long-range ionic motion between the electrodes.

2.3.2. Self-Diffusion of Ions

NMR diffusometry experiments were performed in order to complement the non-selectivity of ionic conductivity measurements and hence understand the fate of the single ions, that is, the imidazolium cation, the TFSI anion, and the Li cation. The ^1H , ^{19}F , and ^7Li nuclei were hence probed and the respective self-diffusion coefficients were estimated at various temperatures, ranging from 293 to 343 K. The self-diffusion coefficients of the Li ions could not be measured for samples with a SIL content less than 60 wt%, due to too short relaxation times. A bipolar gradient NMR pulse sequence was used to eliminate magnetic susceptibility effects that can occur in heterogeneous materials. It must be emphasized that, given the biphasic systems studied, the wide pore size distribution, and the defined experimental conditions, the estimation is limited to apparent self-diffusion coefficients.

The intensity decay of all NMR signals showed a monoexponential character, except for the ^1H signals of samples DMA_{0.4}SIL_{0.6} and DMA_{0.3}SIL_{0.7}, which could also be fitted by a biexponential function (The self-diffusion coefficients extracted from the biexponential fitting can be found in Figure S6, Supporting Information. Moreover, a rough estimate of the fraction of “faster” and “slower” ions has been done (Figure S7,

Supporting Information), showing that the “faster” ions make up a significant part of the total). However, after careful examination, fittings with a monoexponential function seemed sufficiently precise for describing the compositional trends. The extracted self-diffusion coefficient values are summarized in Table S3, Supporting Information. **Figure 3a–c** summarizes the temperature dependence of the self-diffusion coefficients determined for 1) the imidazolium cation, 2) the TFSI anion, and 3) the Li ions, showing an expected increase with temperature. The estimated self-diffusion coefficients for all three ions increase also with the content of confined liquid electrolyte. This trend is shown in Figure 3d for the arbitrary temperature of 333 K. Moreover, while for the bulk liquid electrolyte the cation displays slightly higher diffusivity than the anion, for all other compositions the opposite is observed. An hypothetical explanation for this twist is the slightly negative charge of the oxygen atoms of DMA, which could have a preferred interaction with the cations and a consequent dynamical slowdown.

Another important observation is that the self-diffusion coefficient of the Li cation, although being about half that of the anion, is within the same order of magnitude (Different Δ values had to be used for different nuclei (i.e., ^1H , ^{19}F , and ^7Li) for experimental reasons. Nevertheless, at high temperature,

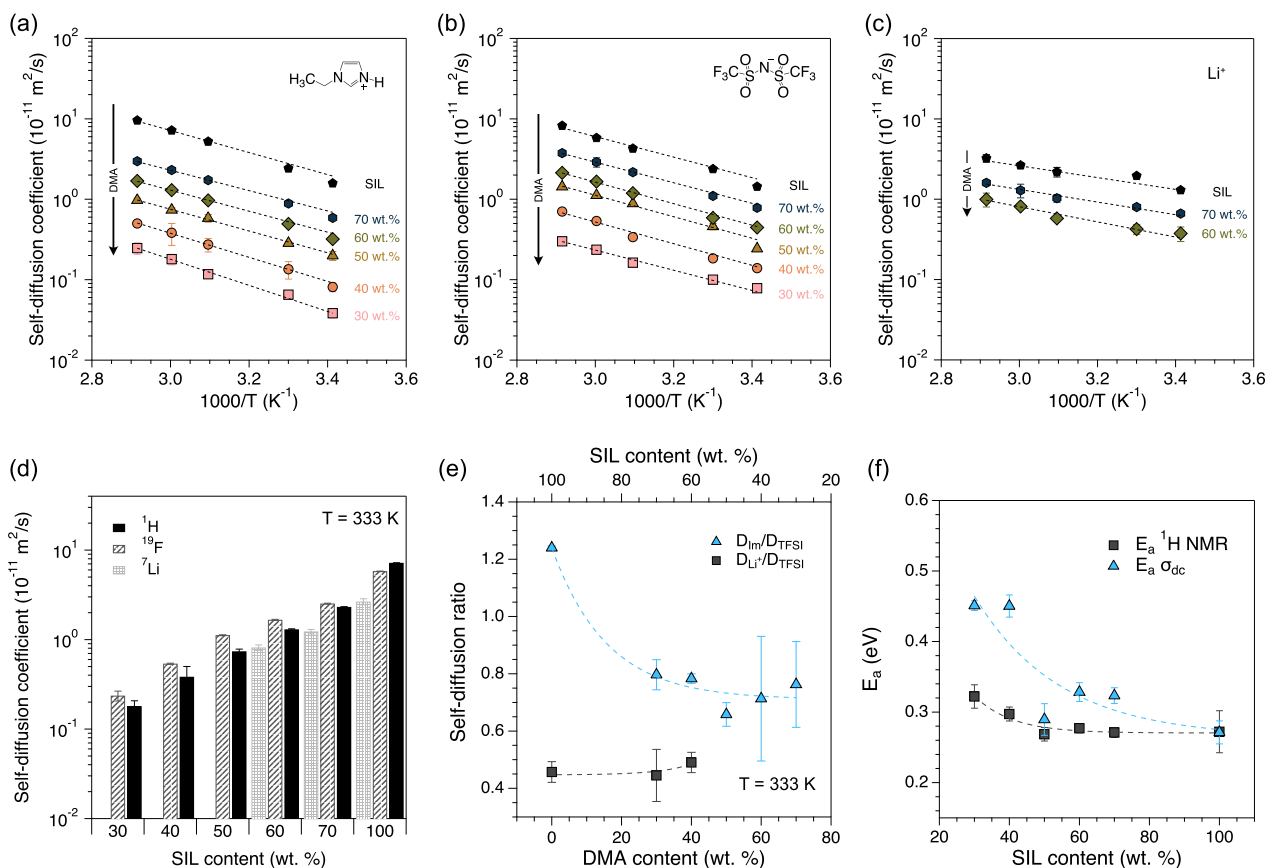


Figure 3. Self-diffusion coefficient of a) the imidazolium cation, b) the TFSI anion, and c) the Li ions (the dashed lines are Arrhenius fits). d) Composition dependence of the self-diffusion coefficients of cations, anions, and Li ions estimated at 333 K. e) Composition dependence of the self-diffusion ratios estimated at 333 K (the associated error bars have been estimated by propagation theory). f) Variation of the activation energy E_a as a function of composition, estimated from an Arrhenius fit of the data in (b) and Figure 2d.

that is, 333 K, the Δ dependence becomes marginal).^[40] Previous studies have reported a lower self-diffusion coefficient for lithium ions in IL-based systems, despite their smaller size.^[41–44] However, these earlier studies primarily focused on aprotic ILs rather than protic ones. The low self-diffusion of the lithium ions can be associated with the interactions that are established between Li^+ and the other components of the system, that is, the TFSI anions and the DMA polymer. This aspect has been investigated by Raman spectroscopy and is discussed further down.

To get further insight into the self-diffusive motion of the various species, the ratios $D_{\text{Im}}/D_{\text{TFSI}}$ and $D_{\text{Li}^+}/D_{\text{TFSI}}$ have been analyzed. Upon confinement, $D_{\text{Im}}/D_{\text{TFSI}}$ decreases smoothly (Figure S9, Supporting Information). Further, while $D_{\text{Li}^+}/D_{\text{TFSI}}$ decreases for $T \leq 323$ K, the opposite seems to be for higher temperatures (Figure S10, Supporting Information). Figure 3e shows the variation of $D_{\text{Im}}/D_{\text{TFSI}}$ and $D_{\text{Li}^+}/D_{\text{TFSI}}$ at $T = 333$ K. The observed confinement effect on the self-diffusion of the cations (Im and Li^+) can be rationalized by their interactions with the slightly negatively charged DMA polymer (in particular the O sites), as discussed earlier. However, the observed increase in the $D_{\text{Li}^+}/D_{\text{TFSI}}$ ratio above 323 K is more difficult to explain, but could possibly be correlated to the increased elasticity of the DMA polymer, based on the observation of $T_{\text{g}}^{\text{DMA}}$ in sample $\text{DMA}_{0.4}\text{SIL}_{0.6}$ at around 320 K.

The activation energy (E_a) of translational motion (ionic conductivity and diffusivity) has been estimated from a common temperature range that does not include phase transitions and is narrow enough to assume an Arrhenius behavior. The temperature range between 293 and 343 K was selected and the experimental values were fitted using the Arrhenius equation (see details in the Figure S11, S12, Supporting Information). Figure 3f shows the E_a estimated from the self-diffusion of the imidazolium cation (^1H) and the E_a estimated from the ionic conductivity data (measured by impedance spectroscopy). The E_a values estimated from the self-diffusion of the TFSI anion and the Li cation are reported in **Table 2**.

Figure 3f reveals that both E_a^{NMR} and $E_a^{\sigma_{\text{dc}}}$ decrease with composition. Moreover, the values of E_a^{NMR} are systematically lower than $E_a^{\sigma_{\text{dc}}}$, likely due to structural inhomogeneities and the fact that diffusivity and conductivity are measured for different spatial scales.^[45] Importantly, the estimated E_a values align with those already reported for other protic ionic liquid systems doped with lithium salts.^[44,46] The observed trend indicates that the ion transport mechanism is restrained by the percolation of

the polymeric network, thereby increasing the energy required for long-range ion motion, while local ion diffusion remains less affected. It is also observed that the activation energy for the Li^+ cation is smaller than for both cations and anions, despite being the slowest species. We have, at present, no explanation for this although one could resort to some previous experimental works speculating on low-dimensional motion or short-range mobility.^[44,47,48]

2.4. Spectroscopically Free Li Ions

Further insight into the nature of intermolecular interactions can appropriately be achieved by Raman spectroscopy. The Raman spectra recorded for the five SBE samples, the neat DMA monomer and the bulk SIL solution, are shown in **Figure 4** in the spectral range from 200 to 1800 cm^{-1} . The lower spectral range, between 240 and 450 cm^{-1} , includes vibrational modes sensitive to conformational changes in TFSI. As previously outlined in the literature, the TFSI anion can adopt either the *cis* or the *trans* conformation, each contributing with distinct, yet energetically close, Raman signatures.^[49,50] The relative intensities in the Raman spectra shown in Figure 4 suggest the simultaneous presence of both conformations; however, a quantitative analysis based on peak fitting with the aim to determine the population of each conformation, was not in the scope of this study.

In all spectra, the strongest vibrational mode is observed at ≈ 743 cm^{-1} , which is attributed to the expansion-contraction mode of the whole TFSI anion (ν_s S-N-S and ν_s CF_3). The position of this strong Raman active mode and its sensitivity to the coordination of the anion has been investigated in pioneering works, by both experiments and theoretical calculations. This mode is typically found in the frequency range 740–744 cm^{-1} for weakly coordinated TFSI anions, while it blueshifts for stronger interactions.^[51–54] In the Raman spectra recorded in this work, this vibration is observed between 742 and 744 cm^{-1} for all samples, implying that the TFSI anions experience spectroscopically weak interactions with their surrounding, regardless of composition.^[46] Importantly, the absence of a Raman peak at higher frequencies (around 748 cm^{-1} , see Figure 4) highlights the absence of spectroscopically strong coordination between Li cations and TFSI anions.^[46] This feature seems to be a specific characteristic of protic ionic liquids.^[8,9] Moreover, by a more detailed peak fitting analysis (Figure S13, Supporting Information), we in fact catch that the main component of this vibration marginally redshifts with the DMA content. This trend is reproduced in Figure 7b (open symbols) and correlates with the enhancement of local dynamics previously observed upon confinement in DMA.^[37]

From the spectral range 1550–1650 cm^{-1} , we have estimated the degree of curing of DMA, by calculating the intensity change of the C–C stretching mode (1640 cm^{-1}) with reference to the C–C stretching mode (1610 cm^{-1}) of the phenyl group that does not take part in the polymerization reaction (see Figure S2, Supporting Information). The degree of curing has been estimated to be around 90%, the limits being 88% for $\text{DMA}_{0.7}\text{SIL}_{0.3}$ and 92% for $\text{DMA}_{0.3}\text{SIL}_{0.7}$.

Table 2. Activation energies (E_a) calculated from temperature-dependent diffusion and conductivity measurements.

Sample	E_a^{NMR} [eV]/ ^1H	E_a^{NMR} [eV]/ ^{19}F	E_a^{NMR} [eV]/ ^7Li	$E_a^{\sigma_{\text{dc}}}$ [eV]
$\text{DMA}_{0.7}\text{SIL}_{0.3}$	0.32 ± 0.02	0.25 ± 0.02	n/a	0.45 ± 0.01
$\text{DMA}_{0.6}\text{SIL}_{0.4}$	0.30 ± 0.01	0.30 ± 0.02	n/a	0.45 ± 0.02
$\text{DMA}_{0.5}\text{SIL}_{0.5}$	0.27 ± 0.01	0.26 ± 0.02	n/a	0.29 ± 0.02
$\text{DMA}_{0.4}\text{SIL}_{0.6}$	0.28 ± 0.01	0.28 ± 0.01	0.19 ± 0.02	0.33 ± 0.01
$\text{DMA}_{0.3}\text{SIL}_{0.7}$	0.27 ± 0.01	0.25 ± 0.11	0.16 ± 0.02	0.32 ± 0.01
SIL	0.28 ± 0.03	0.25 ± 0.03	0.14 ± 0.02	0.27 ± 0.02

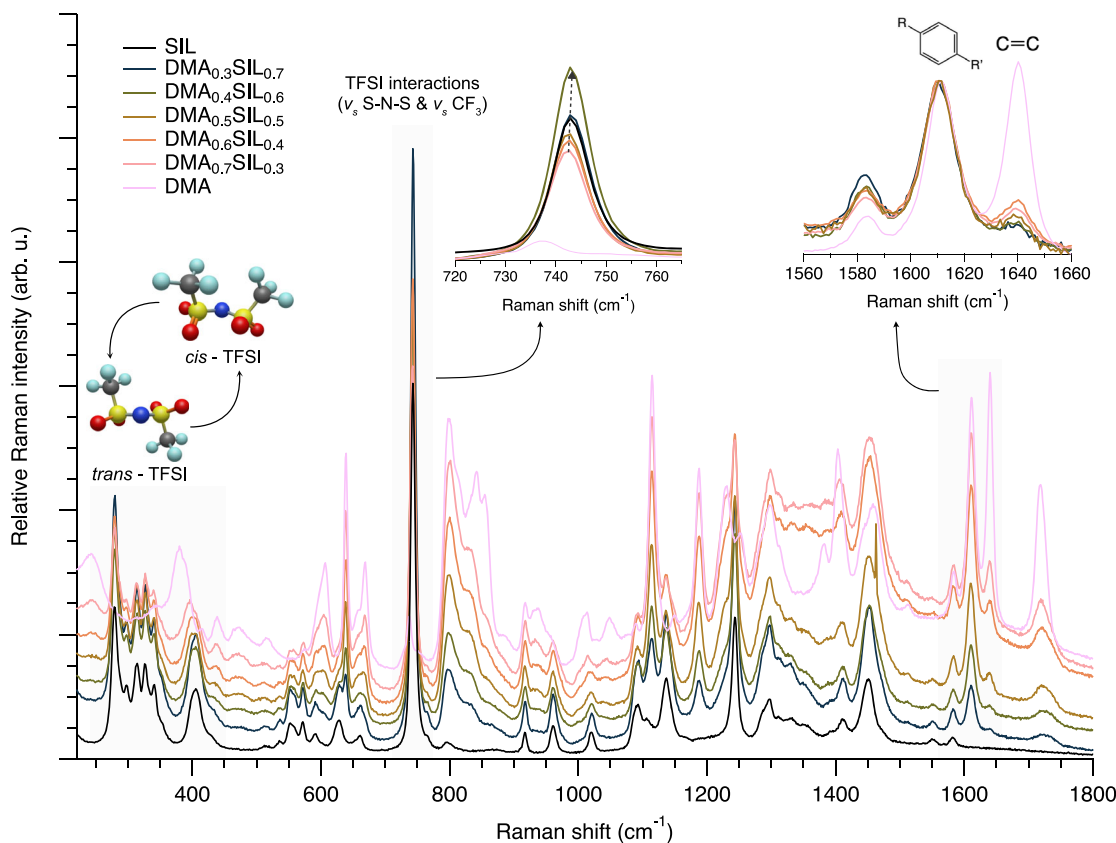


Figure 4. Raman spectra collected at room temperature for the SBE samples having different compositions, the neat monomer (DMA) and the bulk electrolyte solution (SIL) in the 200–1800 cm^{-1} range. The insets show the shift of the intermolecular interaction-sensitive mode (around 742 cm^{-1}), associated with the expansion–contraction mode of the TFSI anion, as a function of the SIL content and the vibrational modes used to estimate the curing rate (1550–1650 cm^{-1}).

2.5. Mechanically Stiffer Membranes upon Confinement

The effect of composition on the mechanical properties of SBEs was evaluated by means of the storage modulus, as reported in

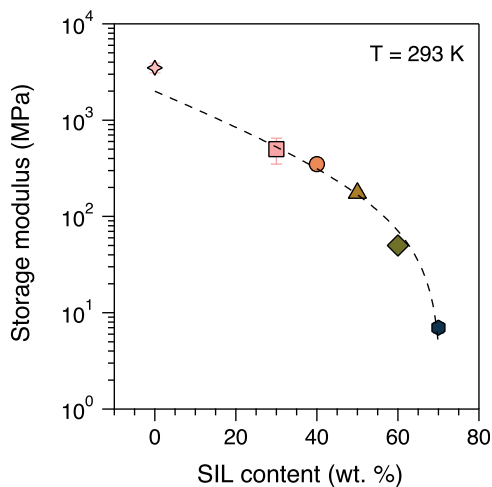


Figure 5. Composition dependence of storage modulus, at $T = 293$ K.

Figure 5. The neat cross-linked DMA exhibits a storage modulus of about 3 GPa at 293 K, while upon increasing SIL content the storage modulus decreases significantly reaching about 10^{-2} GPa for the $\text{DMA}_{0.3}\text{SIL}_{0.7}$ sample (Figure S14, S15, Supporting Information). These findings are in line with previously reported studies of IL-based solid electrolytes and approach the required values for SBEs, that is, 0.5–1 GPa.^[30–36]

2.6. Electrochemical Investigations

The electrochemical stability of the SBEs was first evaluated using linear sweep voltammetry (Figure 6a). The analyzed SBE exhibits a broad electrochemical stability window, from –3 V to at least 6 V (black trace), surpassing the anodic stability of the organic solvent-based SBEs investigated for comparison (dashed blue trace). In fact, the organic solvent-based SBE shows an important rise in the anodic current at 5 V, which can be attributed to the oxidative decomposition of the TFSI anion.^[55]

In addition, a negative half-cell was made using the $\text{DMA}_{0.5}\text{SIL}_{0.5}$ composition and including the carbon fibers to study the electrochemical performance and the suitability for Li-ion battery applications. The cycling voltammetry analysis of the negative half-cells shows a current density of 0.05 A g^{-1}

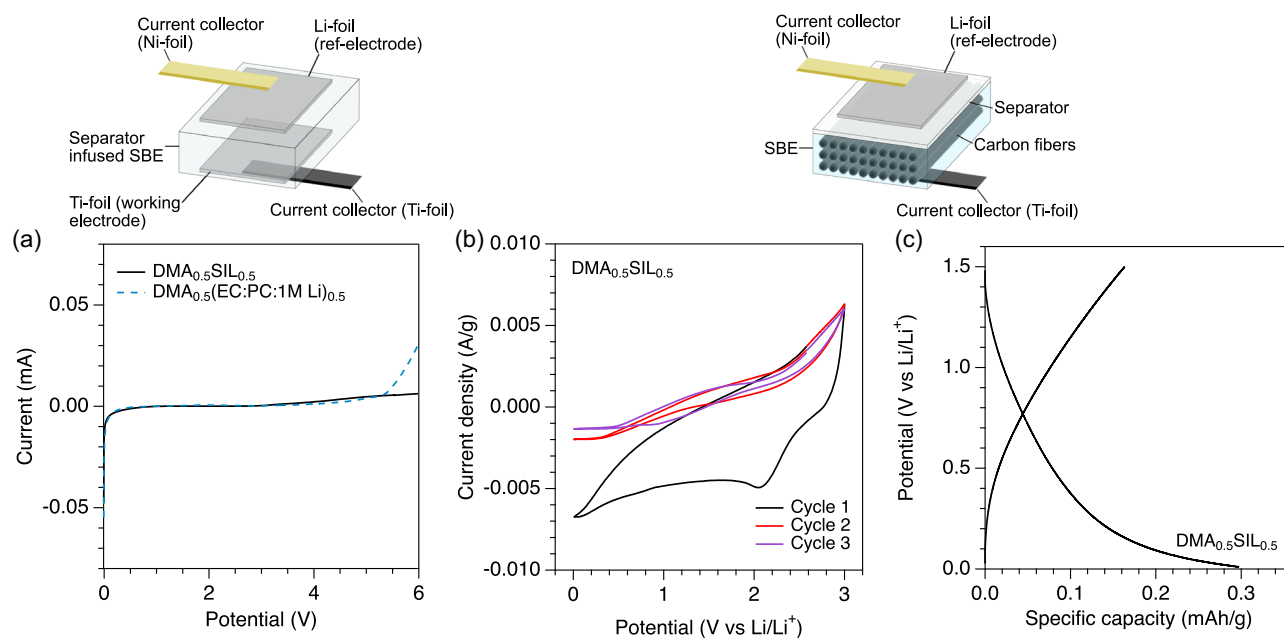


Figure 6. a) Linear sweep voltammetry from 0 to 6 V of $\text{DMA}_{0.5}\text{SIL}_{0.5}$ sample; b) CV at a scan rate of 0.1 mV s^{-1} and c) galvanostatic cycling from 0.01 to 1.5 V. Data in (b) and (c) are for a negative half cell. The illustrations above the figures show the setups used for the measurements.

in a potential range between 0.01 and 3 V, revealing a limited charge storage capacity (Figure 6b). This may result from poor transport properties at the fibers' interface, poor Li-salt content, or limited Li^+ diffusivity.^[56] Galvanostatic cycling was conducted at a current rate of 0.001 mA, corresponding to a practical C-rate of 0.28 C (Figure 6c). The cell shows a moderate specific capacity of 0.3 mAh g^{-1} , supporting the earlier stated hypotheses. To investigate around these hypotheses, we increased the amount of lithium salt in the liquid electrolyte to 0.5 M. Cyclic voltammetry (CV) was then conducted at various scan rates (1–100 mV s^{-1}) over the same voltage range (Figure S17a, Supporting Information), the cell showing a marginal increase in the integrated area with increasing scan rates, indicative of fast electrochemical reactions and a diffusion-controlled process. CV was then run at various potential windows, while keeping the scan rate constant (Figure S17b, Supporting Information), revealing significant reversibility of the half-cell cycles over different potential ranges and quasirectangular symmetric curves. Importantly, no degradation was observed for the electrolyte due to the electrochemical tests.

3. Multifunctionality of SBEs

In order to answer the question of whether an optimal composition exists in protic ionic liquid-based structural battery electrolytes, mechanical, morphological, and transport properties have been thoroughly investigated. None of the properties display a maximum upon changed composition, while all properties change monotonically and some exhibit a mutual correlation. Upon increased DMA content, a gradual decrease in ionic diffusivity is observed, accompanied by an even more pronounced loss in ionic conductivity (Figure 7a). This highlights the

substantial impact of porosity, the presence of dead ends, and poor percolation being detrimental to the long-range motion in these composite materials. In this context, the lower activation energy estimated for the Li ion remains not fully understood and deserves further investigation. Moreover, interaction-sensitive Raman frequencies and glass transition temperatures (T_g) exhibit a consistent trend showing, upon increased DMA content, lower T_g values for the liquid electrolyte and redshifted Raman vibrations of the anion (Figure 7b). This trend supports the hypothesis of increased free volume upon confinement, hence faster local dynamics that correlate with weaker intermolecular interactions. In these biphasic systems, mechanical properties (here storage modulus) are inversely proportional to ionic conductivity (Figure 7c), the target value required for structural battery applications of $\approx 1 \text{ GPa}$ ^[30] being approached at the cost of lower ionic conductivity. Altogether, these findings highlight the fine tunability of properties with composition, the final application determining whether mechanical or transport properties are most important. Among the SBEs studied here, the sample consisting of 50 wt% of SIL seems to exhibit the best compromise between ionic conductivity ($\sigma_{dc} \approx 10^{-1} \text{ mS cm}^{-1}$) and storage modulus (150 MPa), similar to what has been found for equivalent systems based on organic solvents.^[26,27] Proof of concept measurements were therefore performed on $\text{DMA}_{0.5}\text{SIL}_{0.5}$ samples using electrochemical methods. It is found that the electrochemical stability window is very wide and hence useful for practical applications, while tests on half cells indicate moderate specific storage capacity and current density, a challenge to be addressed in upcoming studies. The shape of the CV curves reveals a potential for the use of these structural electrolytes also in supercapacitors.^[57,58] It is emphasized that the high ionic conductivity at high temperatures along with low flammability remain the crucial assets of ionic liquids from the viewpoint

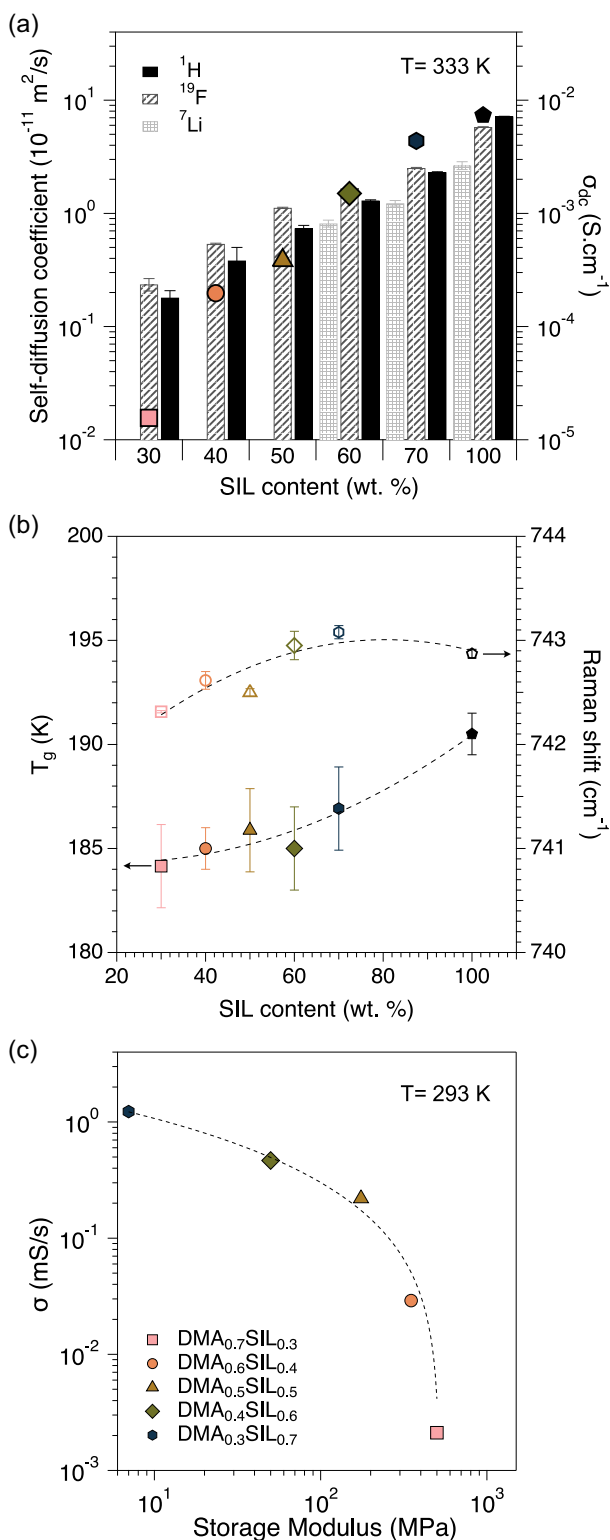


Figure 7. a) Composition dependence of the self-diffusion coefficients (vertical bars) and the ionic conductivity (filled symbols) measured at 333 K. b) Composition dependence of the glass transition temperature of the SIL phase (filled symbols) and the Raman shift of the expansion-contraction mode of the TFSI anion (open symbols). c) Multifunctionality plot of the SBEs (for $T = 293$ K).

of battery safety. Besides, protic ionic liquids offer the added benefit of easier synthesis compared to their aprotic counterparts.

4. Experimental Section

Materials: The monomer, ethoxylated bisphenol A dimethacrylate (DMA, Mw 540 g mol^{-1}), was provided by Sartomer (Arkema Group). The protic ionic liquid 1-ethylimidazolium bis(trifluoromethylsulfonyl) imide ($[\text{C}_2\text{HIm}][\text{TFSI}]$) (V001x102.1.2-IL-0269), 98% purity, was purchased from Iolitec. The lithium bis(trifluoromethane)sulfonimide (LiTFSI) salt (99.95% trace metal basis), the thermal initiator 2,2'-azobis(2-methylpropionitrile) (AIBN), and the organic solvents ethylene carbonate (EC) (battery grade, $\geq 99\%$, acid < 10 ppm, and $\text{H}_2\text{O} < 10$ ppm) and propylene carbonate (PC) (battery grade, $\geq 99\%$, acid < 10 ppm, and $\text{H}_2\text{O} < 10$ ppm) were purchased from Sigma-Aldrich. Polyacrylonitrile (PAN)-based carbon fibers (T800SC-12K-50C) were purchased from Toray Composite Materials America, Inc., and were spread into ultrathin unidirectional (UD) tapes, ≈ 15 mm wide, by Oxeon AB, Sweden. All chemicals were used as received without further treatment.

Synthesis: Structural Battery Electrolyte: Structural battery electrolytes (SBEs) consisting of 1) the ethoxylated bisphenol A dimethacrylate (DMA) network and 2) the liquid electrolyte phase (SIL) were all prepared inside a N_2 filled glovebox (MBRAUN UNILab Plus Eco glovebox, equipped with an MB-LMF II solvent absorber system; ≤ 1 ppm H_2O ; ≤ 1 ppm O_2). The SIL consists of 0.2 M solution in $[\text{C}_2\text{HIm}][\text{TFSI}]$ ionic liquid. It should be mentioned that 0.2 M is the highest concentration of LiTFSI in $[\text{C}_2\text{HIm}][\text{TFSI}]$ achievable by simple mixing overnight. For the synthesis of the solid electrolytes, 1 wt% of the thermal initiator AIBN was mixed with the liquid electrolyte solution in a glass vial. The mixture was then stirred using a vortex apparatus until the complete dissolution of AIBN. Next, the DMA monomer was added to the solution and the mixture was stirred with the vortex apparatus until a homogeneous solution was achieved. The liquid electrolyte content was varied between 0 and 100 wt% of the total weight (i.e., 0, 30, 40, 50, 60, 70, and 100 wt%). The obtained mixture was left to rest for 20 min to allow any trapped air bubbles to escape before being poured onto a borosilicate petri dish. The solution was then cured by radical polymerization on a metallic plate set at 75°C for 180 min (inside the glovebox). The samples are labeled $\text{DMA}_x\text{SIL}_{1-x}$, where $x = 0, 0.3, 0.4, 0.5, 0.6, 0.7, \text{ and } 1$; the neat polymer is labeled DMA while the neat liquid electrolyte is labeled SIL (Table 3).

The synthesis of organic solvent-based SBEs, used as reference samples, was carried out using a 1 M LiTFSI solution from a 50:50 mixture of EC and PC, following a previously described protocol.^[22,26]

Synthesis: Structural Negative Electrode and Half-Cell: Carbon fiber composite negative electrodes were first prepared using a vacuum infusion process. The electrodes were then assembled into half-cells inside a pouch bag with slight adjustments to the procedure previously reported.^[21] Titanium foil (Ti) current collectors were attached to one end of the carbon fibers using conductive silver glue. The vacuum bag assembly was placed on a glass plate, sealed with rubber tape, and dried in a vacuum oven at

Table 3. Quantitative details for the synthesis of the solid structural battery electrolytes.

Sample	SIL [wt%]	m_{DMA} [g]	m_{SIL} [g]	m_{AIBN} [g]
DMA	0.0	1.0	0.0	0.010
DMA _{0.7} SIL _{0.3}	30.0	1.4	0.6	0.014
DMA _{0.6} SIL _{0.4}	40.0	1.2	0.8	0.012
DMA _{0.5} SIL _{0.5}	50.0	1.0	1.0	0.010
DMA _{0.4} SIL _{0.6}	60.0	0.8	1.2	0.008
DMA _{0.3} SIL _{0.7}	70.0	0.6	1.4	0.006
SIL	100.0	0.0	1.0	0.000

50 °C for 12 h. The structural battery electrolyte (SBE) solution, previously prepared in a glovebox, was loaded into a syringe and connected to the vacuum bag inlet for infusion. The infusion process was conducted under a pressure of -0.5 bar, controlled using a vacuum valve. After infusion, the SBE was cured at 90 °C for 45 min. The cured carbon fiber lamina was then sealed in a two-electrode aluminum pouch bag. A lithium metal foil served as the counter and reference electrode, utilizing a nickel current collector, while a Whatman glass microfibre filter acted as a separator between the electrodes. Additional 200 μL of liquid electrolyte was added to the cell to wet the separator film, enhancing the ion conduction.

Characterization: Thermogravimetric Analysis (TGA): TGA experiments were carried out on a Mettler Toledo TGA/DSC3+, equipped with an auto-sampler. Approximately 20 mg of the sample was weighed using a Mettler Toledo XS105 semimicro balance and placed in a 70 μL aluminum crucible, which was capped by a lid with a pinhole. The samples were analyzed under air flow (60 $\mu\text{L min}^{-1}$) covering the temperature range from 25 to 800 °C and using a heating rate of 10 K min^{-1} .

Characterization: Scanning Electron Microscopy: SEM images were recorded using a Zeiss Ultra 55 FEG microscope. Before collecting the SEM images, the samples were washed with ethanol using a Soxhlet apparatus for 24 h to extract the liquid electrolyte phase. Then, samples were gold coated using Leica EM TXP equipment. The gold coating layer was ≈ 4 nm thick, while the diameter of the gold nanoparticles was around 6 nm.

Characterization: Nitrogen Sorption: Nitrogen sorption isotherms were recorded at 77 K using a Micromeritics TriStar volumetric apparatus. Doses of N_2 were added in a measurement cell after an outgassing treatment of the extracted samples at 80 °C, under mild vacuum overnight. The BET surface area of each sample was determined using the Brunauer–Emmett–Teller (BET) method^[59] in the linear range of the isotherms, typically at $p/p_0 = 0.05–0.15$. The pore size distribution was calculated using the Barret–Joyner–Halenda (BJH) method^[60] from the adsorption isotherm. The pore volumes are the cumulative volume of pores with diameters between 0.5 and 300 nm, determined using the BJH method upon adsorption.

Characterization: Calorimetric Measurements: DSC measurements were performed using a Q2000 (TA Instruments) calorimeter, equipped with a liquid nitrogen cooling system (LNCS). Samples of a mass between 10 and 14 mg were encapsulated in a hermetic aluminum crucible. An empty aluminum crucible was used as a reference. The cooling and heating rates were set to 10 K min^{-1} , whereas the covered temperature ranges from 153 to 333 K. The melting (T_m) and glass transition (T_g) temperatures were extracted from the second heating scan. Prior to the measurement, the calorimeter was calibrated to ensure optimal performance. The precalibration procedure involved 1) cleaning the cell, 2) conditioning the cell to create an inert atmosphere using helium gas, and 3) calibrating the LNCS baseline. Subsequently, a three-point calibration using indium ($T_m = 428.8$ K, $\Delta H_m = 28.71$ J g^{-1}), mercury ($T_m = 234.32$ K, $\Delta H_m = 11.443$ J g^{-1}), and MilliQ water ($T_m = 273.15$ K, $\Delta H_m = 335$ J g^{-1}) was carried out for the calibration of enthalpy and transition temperatures. Finally, a baseline measurement was conducted with an empty cell to confirm the successful calibration of the instrument. Regarding the heat capacity calibration, a temperature-modulated differential scanning calorimetry (TM-DSC) calibration was carried out using a sapphire standard. The weighting of the samples, pans, and lids was performed using a balance (Precisica 262SMA-FR) with a 0.01 mg precision.

To determine the glass transition temperature of the liquid phase in SBEs with low SIL content, temperature-modulated DSC measurements were carried out within the temperature range from 160 to 220 K. In TM-DSC, a low-frequency sinusoidal perturbation is added to the standard DSC profile, according to $T = T_0 + \beta \cdot t + \sin(\omega \cdot t)$, where β is the linear cooling/heating rate, t is the time, T is the amplitude, and ω is the angular frequency. An amplitude of 1 K and a period of modulation of 100 s have been used. The corresponding linear heating rate was set to 2 K min^{-1} .

Characterization: Diffusion NMR: To determine the self-diffusion coefficients, NMR experiments were performed using an AVANCE III HD Bruker NMR spectrometer, operating at 14.1 T and equipped with a Diff30 probe connected to a 60 A gradient amplifier. RF coil inserts of a 5 mm 1H/2H double coil, a 5 mm 19F single coil, and a 5 mm 7Li single

coil configuration were used. The self-diffusion coefficients of the different species, that is, imidazolium cation (^1H), TFSI anion (^{19}F), and Li cation (^7Li), in the SBEs were determined at five different temperatures ranging from 293 to 343 K.

Self-diffusion measurements on the SBE samples: The precursor mixture was transferred to 5 mm NMR tubes prior to curing, and then, the samples were heat cured in the NMR tubes. The synthesis and sealing of the samples took place in a glovebox. The self-diffusion coefficients of the different species (imidazolium cation, TFSI anion, and Li cation) in the SBEs were measured using a bipolar field gradient NMR sequence (diffsteBp), in order to suppress the magnetic field susceptibilities induced at the SIL/DMA interfaces that would otherwise contribute to the estimated self-diffusion values.^[61]

Self-diffusion measurements on the bulk liquid electrolyte (SIL): A 5 mm NMR tube was filled with the liquid sample and sealed in the glovebox. A regular stimulated echo NMR sequence (diffste) was used, at room temperature.^[62] However, a double-stimulated echo NMR sequence (diffDste) was employed at higher temperatures, to ensure that thermal convection did not affect the results.^[63]

^1H experiments: A 18 μs 90-degree pulse, 0.05 s acquisition time, 5 s recycling delay, 100 ms diffusion delay (Δ), and 2 ms gradient pulse duration (δ) were used. The maximum gradient strength (g) varied in the range 300–1200 Gauss cm^{-1} while keeping k constant (1.4×10^8) (Equation (2)). The consistency of the measured self-diffusion coefficient values was calibrated against the ^1HDO trace signal in D_2O reference sample.^[64] The constant k is defined as

$$k = (\delta \cdot \gamma \cdot g)^2 (\Delta - \delta/3) \quad (2)$$

where Δ is the diffusion delay time, δ is the gradient pulse duration, γ is the gyromagnetic ratio of the studied nucleus, and g is the gradient strength.

^{19}F experiments: The 90-degree pulse was set to 14 μs , the acquisition time was 0.2 s, and the recycling delay was 2 s. The diffusion delay (Δ) was set to 100 ms, the gradient pulse duration (δ) to 2 ms, and the maximum gradient strength (g) to 1200 Gauss cm^{-1} . The measured self-diffusion coefficient values for ^{19}F were calibrated to a reference sample of hexafluorobenzene (C_6F_6).^[64]

^7Li experiments: A 11 μs 90-degree pulse, 0.1 s acquisition time for SBE samples and 0.4 s for bulk liquid electrolyte, 1.7 s recycle delay, 200 ms diffusion delay (Δ), 0.6 ms gradient pulse duration (δ), and 1700 Gauss cm^{-1} maximum gradient strength (g) were used. Self-diffusion coefficients for Li ions could not be measured for samples with SIL content less than 60 wt%, due to too fast relaxation. All ^7Li self-diffusion coefficient values were referenced to a standard sample of LiCl in H_2O .^[64] All set temperatures were calibrated using the chemical shift differences in pure methanol^[65] or pure ethylene glycol^[66] prior to, and after, the experiments.

Regarding the NMR signals used to follow the intensities' attenuation, the average of the four NMR signals has been considered in the ^1H spectrum for the imidazolium cation, that is, $^1\text{H} -\text{CH}_3$ around 1.2 ppm, $^1\text{H} -\text{CH}_2$ around 4.0 ppm, and ^1H ring at 7.1 and 8.3 ppm, whereas the signal at -80 ppm has been appointed in the ^{19}F spectrum, for the TFSI anion, and the signal around -0.5 ppm has been considered in the ^7Li spectrum, for the Li cation. It is important to point out that the self-diffusion coefficient values for the four different hydrogen atoms were very close (Figure S5, Supporting Information), which is expected since they belong to the same molecular species. However, the self-diffusion coefficient of the exchangeable proton $-\text{NH}$ was not included in the average, as it may participate in exchange events. The intensities of the assigned signals were plotted against k (Equation (2)). Most of the signals' attenuation in this study displayed a monoexponential behavior. The self-diffusion coefficients were then calculated by fitting the decay curves using the Levenberg–Marquart expression

$$I(k) = I_0 \cdot \exp(-k \cdot D) \quad (3)$$

where $I(k)$ is the NMR signal intensity at a certain k , I_0 is the intensity at zero applied gradient strength, and D is the self-diffusion coefficient.

The error bars reported in Figure 3 represent the standard deviation of the apparent self-diffusion coefficient from the four individual self-diffusion coefficients of the different protons for the ^1H diffusion, whereas they represent the error on the fitting for ^{19}F and ^7Li diffusion. Importantly, the ^1H signal attenuation for the $\text{DMA}_{0.4}\text{SiL}_{0.6}$ and $\text{DMA}_{0.3}\text{SiL}_{0.7}$ samples can be fitted by a slight biexponential pattern. Two self-diffusion coefficients were hence calculated using a biexponential equation (see the Supporting Information). Moreover, to examine the dependence of the self-diffusion coefficients on Δ in the studied solid porous SBEs, diffusion NMR experiments were carried out on the $\text{DMA}_{0.4}\text{SiL}_{0.6}$ sample for different Δ values (25, 100, 400, and 1000 ms) (Figure S8, Supporting Information).

Characterization: Raman Spectroscopy: Raman spectra were recorded using a Renishaw InVia Reflex Raman spectrophotometer equipped with an air-cooled CCD detector and a 785 nm wavelength diode laser as the excitation source. The use of this monochromatic light with 1200 grooves mm^{-1} grating achieved a nominal spectral resolution of less than 1 cm^{-1} . The laser power was set to 10% of its maximum value, which is nominally 300 mW at the source. The Raman spectra of SBEs were collected at ambient condition, covering the $100\text{--}4000\text{ cm}^{-1}$ spectral range. Recorded spectra were accumulated by 10 scans with an acquisition time of 10 s each. Before each measurement, the spectrophotometer was calibrated to the first-order vibrational mode of a Si wafer centered at 520.6 cm^{-1} . The raw Raman spectra were treated by excluding sharp signals coming from cosmic rays. For further analysis, and to estimate integrated areas, a multi-peak fit procedure based on a linear background and Voigt functions was applied using the Igor Pro 9 software. In the fitting procedure, the width and position of the Voigt components were not subjected to any constraints.

Characterization: Dielectric Spectroscopy: The conductivity data were collected using a Novocontrol GmbH broadband dielectric spectrometer. Solid SBEs were first coated with a silver paste to ensure good contact with the stainless-steel electrodes. The thickness of the samples was set to $100\text{ }\mu\text{m}$ using Teflon spacers. Measurements were conducted in the frequency range from 10^{-2} to 10^7 Hz , within the temperature range $173\text{--}393\text{ K}$. Conductivity was measured every 5 K with a stabilization time of 600 s at each temperature. A low-voltage electric field of 0.01 V was employed to reduce electrode polarization effects. The temperature was controlled using a nitrogen gas cryostat, with a stability of 0.1 K. The complex conductivity function, $\sigma^*(\omega)$; the complex dielectric permittivity, $\epsilon^*(\omega)$; and the complex electric modulus, $M^*(\omega)$, were collected and analyzed.

Characterization: Rheology: The mechanical properties of the samples were measured using an Anton Paar MCR 302 rheometer, with a plate–plate geometry. The plate diameter was 8 mm. The samples were placed on the bottom plate, before bringing the upper plate into contact and adjusting the thickness between the two plates. The temperature of the measuring cell was controlled with an Anton Paar cooling circulator that allows maintaining the temperature constant within $\pm 0.1\text{ K}$. The linear viscoelastic regime was identified through the strain amplitude dependence of the complex shear modulus, $|G^*(\omega)|$, at $\omega = 10\text{ rad s}^{-1}$, before each measurement. Two types of oscillatory measurements were performed: 1) temperature ramps under isochronal conditions ($\omega = 10\text{ rad s}^{-1}$) at the temperature range between 293 and 373 K and 2) frequency sweeps within the range of $10^{-1} < \omega < 10^2\text{ rad s}^{-1}$, at 293 K.

Characterization: Linear Sweep Voltammetry: The electrochemical stability window was analyzed using linear sweep voltammetry using a Biologic SP-300 battery tester. Two identical pouch bags were assembled for each electrolyte using lithium foil as counter/reference electrode and titanium foil as a working electrode. A Whatman glass microfiber separator, infused with SBE solution and cured following the previously described protocol,^{122,26} was placed between the electrodes. The ionic conductivity of the obtained composite was measured and found comparable to that of the SBE studied, confirming that the use of the Whatman separator does not disrupt the network percolation (Figure S16c, Supporting Information). The experiment was performed with Ti/SBE infused Whatman separator/Li in pouch cell and the linear sweep voltammetry was carried out from 0 to 6 V vs Li/Li⁺ with a scan rate of 1 mV s^{-1} .

Characterization: Electrochemical Analysis: The Bio-Logic SP-300 station was used to perform CV, galvanostatic charge/discharge (GCD), and electrochemical impedance spectroscopy (EIS) on the half-cells. CV tests were performed at various scan rates ranging from 1 to 100 mV s^{-1} and from 0.01 to 3 V vs Li/Li⁺. The electrochemical window was further investigated by performing CV tests in different voltage ranges, with a scan rate of 100 mV s^{-1} . GCD cycles were carried out from 0.01 to 1.5 V at a current of 0.001 mA for 6 cycles, calculated based on the theoretical capacity of graphite. EIS measurements were carried out from 100 kHz to 100 mHz using an alternating current (AC). The specific capacity of the samples was determined from discharge curves using the formula $Q = \int I dt / m$, where Q is the specific capacity in mAh g^{-1} based on the mass of the active material, I is the current, and m is the mass of the carbon fiber active material (g) over time (dt).

Supporting Information

Supporting Information is available from the Wiley Online Library or from the author.

Acknowledgements

N.A., A.P., J.S., and A.M. kindly thank the Area of Advance Materials Science at Chalmers University of Technology for the fund. J.X. and L.E.A. acknowledge 2D TECH VINNOVA Competence Center, Contract 2019-0006; the United States Air Force (USAF), USA, award no. FA8655-21-1-7038; and the Office of Naval Research (ONR), USA, award no. N62909-22-1-2037 for funding this research. R.C. and L.E.A. acknowledge the Wallenberg Initiative Materials Science for Sustainability (WISE) through the Knut and Alice Wallenberg Foundation for the provided fund. The authors thank the Surface Area and Porosity Laboratory at Chalmers University of Technology for the sorption measurement time. The authors thank as well the Swedish NMR center in Gothenburg for the allocated NMR time. The authors thank Prof. Andrea Mele, Dr. Franca Castiglione, and Dr. Maria Enrica di Pietro at Politecnico di Milano for fruitful discussion of NMR results.

Conflict of Interest

The authors declare no conflict of interest.

Author Contributions

Nicole Abdou: data curation (equal); formal analysis (equal); investigation (equal); methodology (equal); visualization (lead); writing—original draft (lead); writing—review and editing (lead). **Achilleas Pipertzis:** data curation (equal); formal analysis (equal); investigation (equal); methodology (equal); validation (equal); writing—review and editing (equal). **Richa Chaudhary:** data curation (equal); formal analysis (equal); investigation (supporting); validation (equal); writing—review and editing (equal). **Lars Evenäs:** formal analysis (supporting); investigation (supporting); validation (equal); writing—review and editing (equal). **Johanna Xu:** formal analysis (supporting); validation (equal); writing—review and editing (equal). **Leif E. Asp:** conceptualization (lead); validation (equal); writing—review and editing (equal). **Jan Swenson:** conceptualization (supporting); funding acquisition (equal); methodology (equal); project administration (equal); supervision (equal); validation (equal); writing—review and editing (equal). **Anna Martinelli:** conceptualization (supporting); funding acquisition (equal); methodology (equal); project administration (equal); supervision (equal); validation (equal); writing—original draft (equal); writing—review and editing (equal).

Data Availability Statement

The data that support the findings of this study are available from the corresponding author upon reasonable request.

Keywords

cross-linked polymers, energy materials, Li ion, mechanical properties, protic ionic liquids, thermal properties, transport properties

Received: January 7, 2025

Revised: February 10, 2025

Published online:

- [1] P. I. Walden, *Bull. Acad. Impér. Sci.* **1914**, 8, 405.
- [2] Z. Lei, B. Chen, Y.-M. Koo, D. R. MacFarlane, *Chem. Rev.* **2017**, 117, 6633.
- [3] T. Vogl, P. Goodrich, J. Jacquemin, S. Passerini, A. Balducci, *J. Phys. Chem. C* **2016**, 120, 8525.
- [4] D. R. MacFarlane, N. Tachikawa, M. Forsyth, J. M. Pringle, P. C. Howlett, G. D. Elliott, J. H. Davis, M. Watanabe, P. Simon, C. A. Angell, *Energy Environ. Sci.* **2014**, 7, 232.
- [5] M. Watanabe, *Electrochemistry* **2016**, 84, 642.
- [6] T. L. Greaves, C. J. Drummond, *Chem. Rev.* **2015**, 115, 11379.
- [7] J.-P. Belieres, C. A. Angell, *J. Phys. Chem. B* **2007**, 111, 4926.
- [8] T. Stettner, A. Balducci, *Energy Storage Mater.* **2021**, 40, 402.
- [9] T. Vogl, S. Menne, R.-S. Kühnel, A. Balducci, *J. Mater. Chem. A* **2014**, 2, 8258.
- [10] E. M. Morais, I. Abdurrokhman, A. Martinelli, *J. Mol. Liq.* **2022**, 360, 119358.
- [11] M. A. B. H. Susan, T. Kaneko, A. Noda, M. Watanabe, *J. Am. Chem. Soc.* **2005**, 127, 4976.
- [12] A. K. Tripathi, *Mater. Today Energy* **2021**, 20, 100643.
- [13] T. Stettner, G. Lingua, M. Falco, A. Balducci, C. Gerbaldi, *Energy Technol.* **2020**, 8, 2000742.
- [14] J. Tan, X. Ao, A. Dai, Y. Yuan, H. Zhuo, H. Lu, L. Zhuang, Y. Ke, C. Su, X. Peng, B. Tian, J. Lu, *Energy Storage Mater.* **2020**, 33, 173.
- [15] Q. Zhang, K. Liu, F. Ding, X. Liu, *Nano Res.* **2017**, 10, 4139.
- [16] A. Hosseinioun, P. Nürnberg, M. Schönhoff, D. Diddens, E. Paillard, *RSC Adv.* **2019**, 9, 27574.
- [17] G. de Araujo Lima e Souza, M. E. di Pietro, F. Castiglione, P. Fazio Martins Martinez, C. C. Fraenza, P. Stallworth, S. Greenbaum, A. Triolo, G. Battista Appetecchi, A. Mele, *Electrochim. Acta* **2024**, 474, 143466.
- [18] L. D. McIntosh, M. W. Schulze, M. T. Irwin, M. A. Hillmyer, T. P. Lodge, *Macromolecules* **2015**, 48, 1418.
- [19] L. E. Asp, M. Johansson, G. Lindbergh, J. Xu, D. Zenkert, *Funct. Compos. Struct.* **2019**, 1, 042001.
- [20] L. E. Asp, K. Bouton, D. Carlstedt, S. Duan, R. Harnden, W. Johannisson, M. Johansen, M. K. G. Johansson, G. Lindbergh, F. Liu, K. Peuvot, L. M. Schneider, J. Xu, D. Zenkert, *Adv. Energy Sustainability Res.* **2021**, 2, 2000093.
- [21] R. Chaudhary, A. Chetry, J. Xu, Z. Xia, L. E. Asp, *Adv. Sci.* **2024**, 11, 2404012.
- [22] R. Chaudhary, J. Xu, Z. Xia, L. E. Asp, *Adv. Mater.* **2024**, 36, 2409725.
- [23] H. Wu, L. Wei, W. Li, C. Shi, X. Yao, Q. Fu, H. Li, X. Guo, *Adv. Funct. Mater.* **2024**, 34, 2403729.
- [24] D. Carlstedt, L. E. Asp, *Composites, Part B* **2020**, 186, 107822.
- [25] J. F. Snyder, R. H. Carter, E. D. Wetzel, *Chem. Mater.* **2007**, 19, 3793.
- [26] N. Ihrner, W. Johannisson, F. Sieland, D. Zenkert, M. Johansson, *J. Mater. Chem. A* **2017**, 5, 25652.
- [27] L. M. Schneider, N. Ihrner, D. Zenkert, M. Johansson, *ACS Appl. Energy Mater.* **2019**, 2, 4362.
- [28] T. Jin, G. Singer, K. Liang, Y. Yang, *Mater. Today* **2023**, 62, 151.
- [29] F. Danzi, R. M. Salgado, J. E. Oliveira, A. Arteiro, P. P. Camanho, M. H. Braga, *Molecules* **2021**, 26, 8.
- [30] N. Shirshova, A. Bismarck, S. Carreyette, Q. P. V. Fontana, E. S. Greenhalgh, P. Jacobsson, P. Johansson, M. J. Marczewski, G. Kalinka, A. R. J. Kucernak, J. Scheers, M. S. P. Shaffer, J. H. G. Steinke, M. Wienrich, *J. Mater. Chem. A* **2013**, 1, 15300.
- [31] S. J. Kwon, T. Kim, B. M. Jung, S. B. Lee, U. H. Choi, *ACS Appl. Mater. Interfaces* **2018**, 10, 35108.
- [32] F. Gayet, L. Viau, F. Leroux, F. Mabile, S. Monge, J.-J. Robin, A. Vioux, *Chem. Mater.* **2009**, 21, 5575.
- [33] K. Matsumoto, T. Endo, *Macromolecules* **2008**, 41, 6981.
- [34] K. Matsumoto, T. Endo, *Macromolecules* **2009**, 42, 4580.
- [35] K. Matsumoto, T. Endo, *J. Polym. Sci., Part A: Polym. Chem.* **2011**, 49, 1874.
- [36] M. W. Schulze, L. D. McIntosh, M. A. Hillmyer, T. P. Lodge, *Nano Lett.* **2014**, 14, 122.
- [37] A. Pipertzis, N. Abdou, J. Xu, L. E. Asp, A. Martinelli, J. Swenson, *Energy Mater.* **2023**, 3, 300050.
- [38] I. Abdurrokhman, K. Elamin, O. Danyliv, M. Hasani, J. Swenson, A. Martinelli, *J. Phys. Chem. B* **2019**, 123, 4044.
- [39] G. Yu, D. Zhao, L. Wen, S. Yang, X. Chen, *AIChE J.* **2012**, 58, 2885.
- [40] T. Ohkubo, K. Kidena, A. Ohira, *Macromolecules* **2008**, 41, 8688.
- [41] N. K. Jayakody, C. C. Fraenza, S. G. Greenbaum, D. Ashby, B. S. Dunn, *J. Phys. Chem. B* **2020**, 124, 6843.
- [42] F. Lundin, A. Idström, P. Falus, L. Evenäs, S. Xiong, A. Matic, *J. Phys. Chem. C* **2022**, 126, 16262.
- [43] V. Piacentini, C. Simari, A. Gentile, S. Marchionna, I. Nicotera, S. Brutti, E. Bodo, *ChemSusChem* **2024**, 17, e202301962.
- [44] G. de Araujo Lima e Souza, M. E. Di Pietro, F. Castiglione, P. Fazio Martins Martinez, M. Middendorf, M. Schönhoff, C. C. Fraenza, P. Stallworth, S. Greenbaum, A. Triolo, G. B. Appetecchi, A. Mele, *Electrochim. Acta* **2024**, 475, 143598.
- [45] J. Rao, X. Wang, R. Yunis, V. Ranganathan, P. C. Howlett, D. R. MacFarlane, M. Forsyth, H. Zhu, *Electrochim. Acta* **2020**, 346, 136224.
- [46] N. Demarthe, L. A. O'Dell, B. Humbert, R. D. Arrua, D. Evans, T. Brousse, J. Le Bideau, *Adv. Energy Mater.* **2024**, 14, 2304342.
- [47] K. Volgmann, V. Epp, J. Langer, B. Stanje, J. Heine, S. Nakhal, M. Lerch, M. Wilkening, P. Heitjans, *Z. Phys. Chem* **2017**, 231, 1215.
- [48] A. Skripov, G. Majer, O. Babanova, R. Skoryunov, A. Soloninin, M. Ley, T. Jensen, S. Orimo, T. Udovic, *Solid State Ionics* **2021**, 362, 115585.
- [49] M. Herstedt, M. Smirnov, P. Johansson, M. Chami, J. Grondin, L. Servant, J. C. Lassègues, *J. Raman Spectrosc.* **2005**, 36, 762.
- [50] A. Martinelli, A. Matic, P. Johansson, P. Jacobsson, L. Börjesson, A. Ferricola, S. Panero, B. Scrosati, H. Ohno, *J. Raman Spectrosc.* **2011**, 42, 522.
- [51] W. Huang, R. Frech, R. A. Wheeler, *J. Phys. Chem.* **1994**, 98, 100.
- [52] R. Arnaud, D. Benrabah, J. Sanchez, *J. Phys. Chem.* **1996**, 100, 10882.
- [53] S. P. Gejji, C. Suresh, K. Babu, S. R. Gadre, *J. Phys. Chem. A* **1999**, 103, 7474.
- [54] Y. Urabayashi, T. Yamaguchi, S. Fukuda, T. Mitsugi, M. Takeuchi, K. Fujii, S.-I. Ishiguro, *Anal. Sci.* **2008**, 24, 1297.
- [55] S. P. Ong, O. Andreussi, Y. Wu, N. Marzari, G. Ceder, *Chem. Mater.* **2011**, 23, 2979.
- [56] A. Lahiri, T. J. S. Schubert, B. Iliev, F. Endres, *Phys. Chem. Chem. Phys.* **2015**, 17, 11161.
- [57] R. Mysyk, E. Raymundo-Piñero, M. Anouti, D. Lemordant, F. Béguin, *Electrochem. Commun.* **2010**, 12, 414.

- [58] N. C. Osti, K. Liang, K. Prenger, B. P. Thapaliya, M. Tyagi, S. Dai, M. Naguib, E. Mamontov, *APL Energy* **2024**, *2*, 046101.
- [59] S. Brunauer, P. H. Emmett, E. Teller, *J. Am. Chem. Soc.* **1938**, *60*, 309.
- [60] E. P. Barrett, L. G. Joyner, P. P. Halenda, *J. Am. Chem. Soc.* **1951**, *73*, 373.
- [61] R. Cotts, M. Hoch, T. Sun, J. Markert, *J. Magn. Reson.* **1989**, *83*, 252.
- [62] J. E. Tanner, *J. Chem. Phys.* **1970**, *52*, 2523.
- [63] A. Jerschow, N. Müller, *J. Magn. Reson.* **1997**, *125*, 372.
- [64] M. Holz, H. Weingartner, *J. Magn. Reson.* **1991**, *92*, 115.
- [65] M. Findeisen, T. Brand, S. Berger, *Magn. Reson. Chem.* **2007**, *45*, 175.
- [66] Bruker Inc., Variable Temperature Control for NMR Probes **2022**.